

Comparison between resistive and collisionless double tearing modes for nearby resonant surfaces

Andreas Bierwage^{1,*} and Qingquan Yu^{1,†}

¹*Max-Planck-Institut für Plasmaphysik, IPP-Euroatom Association, 85748 Garching, Germany*[‡]

(Dated: February 9, 2020)

The linear instability characteristics and nonlinear dynamics of collisional (resistive) and collisionless (electron inertia) double tearing modes (DTMs) are compared using a reduced cylindrical model of a tokamak plasma. We focus on cases where two $q = 2$ resonant surfaces are located a small distance apart. It is found that regardless of the magnetic reconnection mechanism, resistivity or electron inertia, the dominant modes are those with high poloidal mode numbers $m \sim 10$. However, the collisionless case tends to have a significantly broader spectrum of unstable modes. In the nonlinear regime, it is shown that in both cases the fast growing high- m DTMs lead to a turbulent collapse in an annular region, whereas small magnetic island structures are formed. In addition, collisionless DTMs exhibit multiple reconnection cycles due to reversibility and strong $\mathbf{E} \times \mathbf{B}$ flows. Collisionless reconnection leads to a saturated stable state, while in the collisional case resistive decay keeps the system weakly dynamic by driving it back towards the unstable equilibrium.

I. INTRODUCTION

Non-monotonic current density profiles, where the maximum current density is located off the magnetic axis, are frequently produced in tokamak plasmas (see Ref. [1] and references therein). These so-called reversed-shear (RS) configurations are of considerable interest for establishing high-performance discharges with improved confinement (e.g., Refs. [2, 3]). The non-monotonic current profile is associated with a safety factor profile $q(r)$ that has a minimum q_{\min} at some radius $r_{\min} > 0$. Around r_{\min} , pairs of magnetic surfaces where q has the same rational value $q_s = m/n$ can occur a small distance D_{12} apart. Under such conditions, coupled resonant perturbations (with poloidal mode number m and toroidal mode number n) known as double tearing modes (DTMs) can become unstable [4, 5].

The DTM is a stronger instability than an ordinary tearing mode [6] and bears similarity with the $m = 1$ internal kink mode [5, 7]. Several nonlinear studies on cases with relatively large inter-resonance distances and dominant low- m modes were conducted in the past (e.g., Refs. [8, 9, 10, 11]). It has recently been shown that DTMs with high poloidal mode numbers $m \sim 10$ are strongly unstable when the distance between the resonances is small [12]. Details about the linear instability characteristics of such cases were presented in Ref. [1] for resistive DTMs.

The present paper is motivated by the question how the linear instability and nonlinear evolution of high- m DTMs, in configurations with small inter-resonance distance D_{12} , depend on the reconnection mechanism. In particular, a comparison is made between collisional and

collisionless DTMs in which magnetic reconnection is mediated by resistivity and electron inertia, respectively. The practical motivation for this work lies in the fact that scenarios with small distance D_{12} inevitably occur during the evolution of the q profile when q_{\min} passes through low-order rational values q_s . Moreover, in tokamak plasmas of interest to thermonuclear fusion applications the classical resistivity is low, so models with collisionless reconnection mechanisms may give a more realistic picture (unless the effective resistivity is much higher than the classical one [13, 14]). The results may thus be useful for understanding magnetohydrodynamic (MHD) activity observed near q_{\min} in RS tokamak configurations [15, 16] and may bear relevance for problems of stability, confinement and current profile control.

Due to similarities between strongly coupled DTMs and $m = 1$ internal kink modes the present work is related to previous studies on fast collisionless reconnection, some of which used a model similar to the reduced set of MHD equations employed here [17, 18, 19]. For the purpose of simplicity and transparency, some potentially important physical effects (e.g., finite-Larmor-radius corrections and diamagnetic drifts [20, 21]) are ignored at the present stage.

In the first part of this paper, it is shown that collisionless DTMs also have a broad spectrum with dominant high- m modes when the inter-resonance distance is small, so they are similar in this respect to resistive DTMs. When resistivity or the electron skin depth are increased, the mode number of the fastest growing mode m_{peak} increases. A significant difference between the two cases is that increasing electron inertia also increases the width of the spectrum, while resistive DTMs tend to have a fixed spectral width.

In the second part, nonlinear simulation results are presented. Both cases, resistive and collisionless, have in common the formation of small magnetic islands, simultaneous reconnection at many locations around the core plasma (annular collapse), and generation of MHD

*Electronic address: abierwag@uci.edu

†Electronic address: qiy@ipp.mpg.de

‡Present address: Department of Physics and Astronomy, University of California, Irvine, CA 92697

turbulence. In addition, the collisionless reconnection scenario has the distinctive feature of being reversible [19]. Together with the high growth rates (which result in strong $\mathbf{E} \times \mathbf{B}$ flows), reversibility allows for multiple reconnection cycles. Secondary reconnection was previously demonstrated for the $m = 1$ internal kink mode [18] and is here shown to occur in similar form with DTMs. It is essentially an overshoot phenomenon and thus much more pronounced in systems where dissipation is weak.

This paper is organized as follows. In Section II the physical model is introduced and Section III contains details on the numerical method employed. In Section IV we describe the equilibrium configuration used and its linear instability characteristics. Nonlinear simulation results are presented in Section V, followed by a discussion and conclusions in Section VI.

II. MODEL

We use a reduced set of magnetohydrodynamic (RMHD) equations in cylindrical geometry in the limit of zero pressure [22, 23]. The RMHD model has proven to be useful in studies of MHD instabilities when the focus is on a qualitative description of fundamental aspects of the magnetized plasma system, as is the case here. We use an Ohm's law that includes resistivity and electron inertia terms,

$$\mathbf{E} - \mathbf{v} \times \mathbf{B} = \eta J + \frac{m_e}{n_e e^2} \frac{dJ}{dt}, \quad (1)$$

where η is the resistivity, n_e the electron density and m_e the electron mass. The RMHD equations govern the evolution of the generalized flux function F and the electrostatic potential ϕ . They are, in normalized form,

$$\partial_t F = [F, \phi] - \partial_\zeta \phi + S_{\text{HP}}^{-1} (\hat{\eta} \nabla_\perp^2 F - E_0) \quad (2)$$

$$\partial_t u = [u, \phi] + [j, \psi] + \partial_\zeta j + R e_{\text{HP}}^{-1} \nabla_\perp^2 u. \quad (3)$$

Here, F is defined in terms of the magnetic flux ψ and current density j as $F \equiv \psi + d_e^2 j$, with $d_e = \sqrt{m_e/(n_e e^2)}$ being the collisionless electron skin depth. The time is measured in units of the poloidal Alfvén time $\tau_{\text{HP}} = \sqrt{\mu_0 \rho_m a / B_0}$ and the radial coordinate is normalized by the minor radius a of the plasma. ρ_m is the mass density and B_0 the strong axial magnetic field. The current density j and the vorticity u are related to ψ and ϕ through $j = -\nabla_\perp^2 \psi$ and $u = \nabla_\perp^2 \phi$, respectively.

The strength of the resistive diffusion term in Eq. (2) is measured by the magnetic Reynolds number $S_{\text{HP}} = \tau_\eta / \tau_{\text{HP}}$, with $\tau_\eta = a^2 \mu_0 / \eta_0$ being the resistive diffusion time and $\eta_0 = \eta(r = 0)$ the electrical resistivity in the plasma core. In fact, this dissipation term has two components: $S_{\text{HP}}^{-1} \nabla_\perp^2 F = -S_{\text{HP}}^{-1} j + d_e^2 \mu_e \nabla_\perp^2 j$. The first part corresponds to the actual resistive dissipation, while $d_e^2 \mu_e \nabla_\perp^2 j$ is a hyper-resistivity term [24]. The coefficient μ_e is interpreted as an (anomalous) perpendicular electron viscosity [25, 26, 27]. Its role in the collisionless reconnection process is to limit the width of the

current sub-layer which otherwise would shrink indefinitely [19]. In our calculations, μ_e has the same value as S_{HP}^{-1} , so $d_e^2 \mu_e \ll S_{\text{HP}}^{-1}$. Nevertheless, in our nonlinear simulations of the collisionless case the magnitude of the electron viscosity term is often measured to be by a factor of order 10 larger than the resistive term due to the higher-order derivative. Flow damping at small scales is provided by an ion viscosity term in Eq. (3). Its strength is determined by the kinematic Reynolds number $Re_{\text{HP}} = a^2 / \nu \tau_{\text{HP}}$, where ν is the perpendicular ion viscosity.

The source term $S_{\text{HP}}^{-1} E_0$ in Eq. (2), with $E_0 = \hat{\eta} \bar{j}$, balances the resistive diffusion of the equilibrium current profile $\bar{j}(r)$. In nonlinear calculations for the collisional case the resistivity profile is given in terms of the equilibrium current density distribution as $\hat{\eta}(r) = \bar{j}(r = 0) / \bar{j}(r)$ (constant loop voltage, $E_0 = \text{const}$). For simplicity, the temporal variation of the resistivity profile $\hat{\eta}$ is neglected. The effect of $S_{\text{HP}} E_0$ is negligible in the collisionless case, and there $\hat{\eta} = 1$ is used.

Each field variable f is decomposed into an equilibrium part \bar{f} and a perturbation \tilde{f} as

$$f(r, \vartheta, \zeta, t) = \bar{f}(r) + \tilde{f}(r, \vartheta, \zeta, t). \quad (4)$$

The system is described in terms of the Fourier modes, $\psi_{m,n}$ and $\phi_{m,n}$, obtained from the expansion

$$f(r, \vartheta, \zeta, t) = \frac{1}{2} \sum_{m,n} f_{m,n}(r, t) e^{i(m\vartheta - n\zeta)} + \text{c.c.}, \quad (5)$$

with m being the poloidal mode number and n the toroidal mode number. The (m, n) subscripts are often omitted for convenience. We consider only the dynamics within a given helicity $h = m/n = \text{const}$, so the problem is reduced to two dimensions.

III. NUMERICAL METHOD

For the numerical solution of the model equations (2) and (3) a two-step predictor-corrector method is applied. In the first time step the dissipation terms are treated implicitly, all others explicitly, and the field variables are estimated at an intermediate time step $t + \Delta t/2$. The second is a full time step, $t \rightarrow t + \Delta t$, with the right-hand sides of Eqs. (2) and (3) evaluated at the intermediate time step $t + \Delta t/2$ estimated before. In the nonlinear regime the time step size is of the order $\Delta t \sim 10^{-3}$.

Up to 128 Fourier modes (including $m = 0$) are carried, while Poisson brackets $[f, g] = \frac{1}{r} (\partial_r f \partial_\vartheta g - \partial_r g \partial_\vartheta f)$ are evaluated in real space (pseudo-spectral technique, dealiased). The radial coordinate is discretized using a non-uniformly spaced grid, with a grid density of up to $N_r^{-1} = 1/6000$ in regions where sharp current density peaks occur. A fourth-order centered finite-difference method is applied for the ∂_r -terms in the Poisson brackets. The Laplacians $\nabla_{\perp(m,n)}^2 = \frac{1}{r} \partial_r r \partial_r - m^2 / r^2$ are eval-

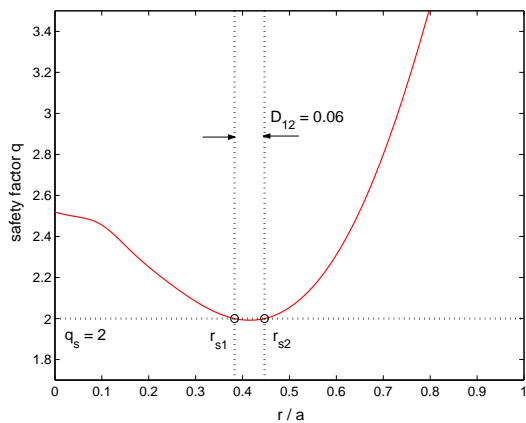


FIG. 1: (Color online). Equilibrium safety factor profile $q(r)$. Resonant surfaces are indicated by vertical dotted lines (distance: $D_{12} = 0.06$).

uated at second-order accuracy (tridiagonal matrix equations).

Periodic boundary conditions are applied in the azimuthal and axial directions. At $r = 1$ an ideally conducting wall is assumed, requiring all perturbations to be identical to zero at that location: $\tilde{f}(r = 1) = 0$ (fixed boundary, no vacuum region). At $r = 0$, additional boundary conditions are applied to ensure smoothness: $\partial_r \tilde{f}_{m=0}(r = 0) = 0$ and $\tilde{f}_{m \neq 0}(r = 0) = 0$.

The linear dispersion relations and mode structures presented in the following section were computed using both an initial-value-problem (IVP) solver (linearized version of the numerical code described above) and an eigenvalue-problem (EVP) solver [1]. The results of both approaches agree. Output data obtained with the EVP solver which the IVP solver cannot produce [such as multiple eigenmodes for a given (m, n)] were verified by checking the numerical convergence with increasing grid density.

IV. EQUILIBRIUM AND LINEAR INSTABILITY

The equilibrium state is taken to be axisymmetric (only $m = n = 0$ components) and free of flows, i.e., $\phi = \bar{u} = 0$. The equilibrium magnetic configuration is uniquely defined in terms of the safety factor $q(r)$. The magnetic flux function and current density profiles are given by the relations

$$q^{-1} = -\frac{1}{r} \frac{d}{dr} \psi_{0,0} \quad \text{and} \quad j_{0,0} = \frac{1}{r} \frac{d}{dr} \frac{r^2}{q}. \quad (6)$$

The form of the q profile is shown in Fig. 1 [36]. The two resonant surfaces under consideration have $q_s \equiv q(r_{si}) = 2$ ($i = 1, 2$). Their distance is $D_{12} = |r_{s2} - r_{s1}| = 0.06$

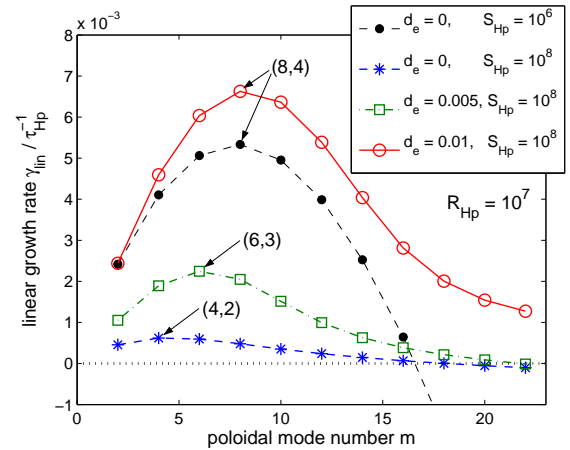


FIG. 2: (Color online). Growth rate spectra $\gamma_{\text{lin}}(m)$ of unstable DTM eigenmodes for the q profile in Fig. 1. The dashed line with filled circles shows the collisional case studied in this paper ($S_{\text{HP}} = 10^6$, $R_{\text{HP}} = 10^7$, $d_e = 0$). For the parameter values $S_{\text{HP}} = 10^8$ and $R_{\text{HP}} = 10^7$, further spectra are shown for $d_e = 0, 0.005$ and 0.01 . The case with $d_e = 0.01$ is the one used in this paper to study the nonlinear evolution of collisionless DTM. Only growth rates on the dominant eigenmode branch ($M^{(2)}$ -type, cf. Fig. 4) are shown. The fastest growing modes are indicated by arrows.

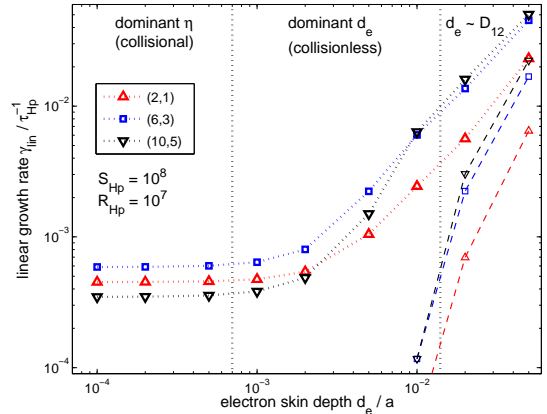


FIG. 3: (Color online). d_e dependence of the linear growth rate of the modes $(m, n) = (2, 1)$, $(6, 3)$ and $(10, 5)$. The scanned range $10^{-4} \leq d_e \leq 5 \times 10^{-2}$ is roughly divided into three regimes: predominantly collisional, collisionless, and a regime where the skin depth d_e becomes comparable to the inter-resonance distance D_{12} . Both eigenmode branches $M^{(1)}$ (dashed lines) and $M^{(2)}$ (dotted lines) are shown (cf. Fig. 4).

and the values of the magnetic shear $s = rq'/q$ at the resonances are $s_1 = -0.10$ and $s_2 = 0.12$.

The linear dispersion relation (spectrum of linear growth rates) $\gamma_{\text{lin}}(m)$ is plotted in Fig. 2 for collisional and collisionless cases. Increasing the electron skin depth d_e increases the linear growth rates, as is to be expected. In addition, an increase in the mode number of the fastest growing mode, m_{peak} , is observed. The results in Fig. 2

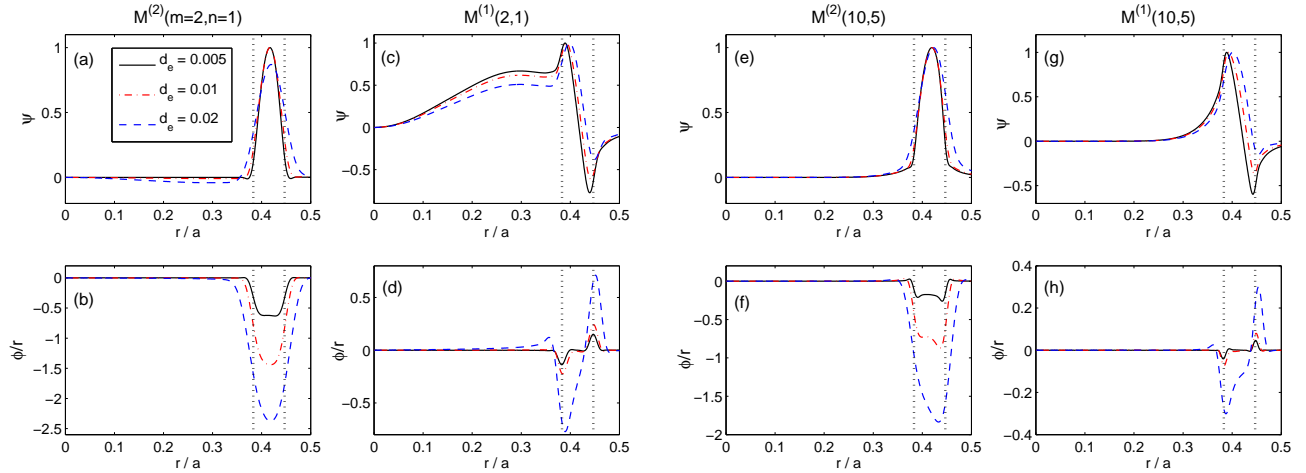


FIG. 4: (Color online). Eigenmode structures for collisionless modes with $(m, n) = (2, 1)$ and $(10, 5)$ in dependence of d_e . The eigenmode of type $M^{(2)}$ (a,b,e,f) is unstable in the whole range of d_e shown in Fig. 3 and has odd parity. $M^{(1)}$ -type modes (c,d,g,h) have even parity and are destabilized when d_e becomes comparable to D_{12} .

show that the dominance of modes with $m > 2$ for small distance D_{12} is a feature common to both collisional [1] and collisionless DTMs.

A remarkable difference between collisional and collisionless DTMs is that m_{\max} , the mode number of the last unstable mode ($g\gamma_{\text{lin}}(m) > 0$ for $m \leq m_{\max}$) increases with increasing d_e , as can be seen in Fig. 2. In the case of collisional DTMs a variation of S_{HP} does not affect m_{\max} (here $m_{\max} = 16$) (cf. also Ref. [1]). This property has the important implication that the instability of a DTM with a given mode number m is not determined by the global current profile. Although, this observation is not yet fully understood, it seems that the detailed structure of the mode near the resonant surfaces also plays a role. Further calculations show that setting the electron viscosity μ_e to zero reduces the growth rates in the high- m domain, but it does not remove the characteristic high- m tail of the collisionless DTM spectrum.

The d_e dependence of the growth rates of individual modes is shown in Fig. 3 for $(m, n) = (2, 1)$, $(6, 3)$ and $(10, 5)$ for $S_{\text{HP}} = 10^8$ and $Re_{\text{HP}} = 10^7$. The collisional regime is identified with the region $d_e \lesssim 7 \times 10^{-4}$. Here the electron inertia plays no significant role. In the range $10^{-3} < d_e \lesssim 10^{-2}$ we speak of collisionless DTMs. Here the growth rates rise steeply with d_e , whereas the $(10, 5)$ mode undergoes the strongest destabilization among the modes plotted. Finally, for $d_e > 10^{-2}$ the skin depth becomes comparable to the inter-resonance distance D_{12} and one may expect that here the nature of the instability changes [28]. In fact, in this regime a second unstable eigenmode arises for each (m, n) (small symbols connected by dashed lines in Fig. 3).

The eigenmode structures for collisionless modes with $(m, n) = (2, 1)$ and $(10, 5)$ are shown in Fig. 4. The $M^{(2)}$ -type mode is the dominant one in the regime considered here. It is similar to its resistive equivalent described in

Ref. [1]. Both have odd parity, meaning that the magnetic islands at r_{s1} are half a wavelength out of phase with those at r_{s2} . The slower $M^{(1)}$ -type mode has even parity (islands in phase). However, in contrast to the even-parity resistive $M^{(1)}$ -type mode [1], which is found in the limit of large D_{12} (and eventually becomes a single tearing mode), the collisionless $M^{(1)}$ -type mode appears in the limit of $D_{12} \sim d_e$ and peaks at both resonant surfaces.

V. NONLINEAR RESULTS

Starting from the unstable equilibrium in Fig. 1, the linear instabilities are excited by applying an initial perturbation of the form

$$\tilde{\psi}(t=0) = \frac{1}{2} \sum_m \Psi_{0,m} r(r-1) e^{im(\vartheta_* + \vartheta_{0,m})} + \text{c.c.}, \quad (7)$$

where $\Psi_{0,m}$ is the perturbation amplitude (collisional case: $\Psi_{0,m} = 10^{-7}$, collisionless case: $\Psi_{0,m} = 10^{-8}$), $\vartheta_* \equiv \vartheta - q_s^{-1}\zeta$ is a helical angle coordinate and $\vartheta_{0,m}$ is an initial phase shift. The values $\vartheta_{0,m} = 0$ or $\vartheta_{0,m} = \pi$ are assigned to each m in a random manner. This introduces some degree of incoherence while retaining mirror symmetry about both the x and the y axis (due to $q_s = 2$ and parity conservation in RMHD). This restriction is applied for convenience and higher numerical accuracy, and has no significant effect on the phenomena discussed in this paper.

The early evolution begins with a linear phase followed by one where low- m modes are nonlinearly driven by the faster high- m modes. These stages were discussed in detail in Refs. [12, 29, 30] and are found to be similar here. Thus, in the following, we focus on the subsequent fully nonlinear regime.

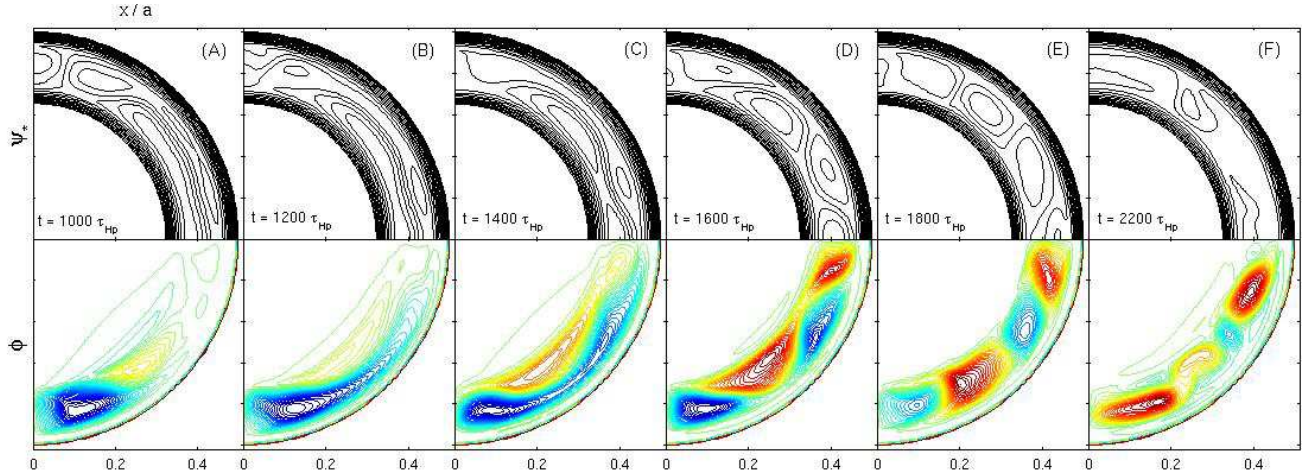


FIG. 5: (Color online). Collisional case. Reconnection dynamics with $q_s = 2$ resistive DTMs for small inter-resonance distance $D_{12} = 0.06$. The six snapshots (A)–(F) were taken during the interval $1000 \leq t \leq 2200$. Each snapshot consists of contour plots of the helical flux $\psi_* = \psi + r^2/(2q_s)$ (top) and the electrostatic potential ϕ (bottom), taken in the poloidal plane at $\zeta = 0$. Parameters: $S_{\text{Hp}} = 10^6$, $Re_{\text{Hp}} = 10^7$, $d_e = 0$.

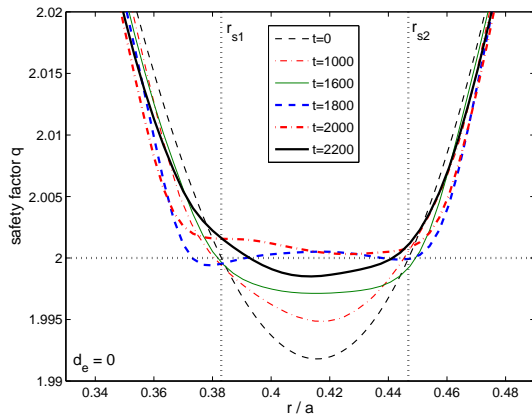


FIG. 6: (Color online). Collisional case. Evolution of the q profile during the annular collapse.

The nonlinear simulation for the collisional case was carried out for the parameter values $S_{\text{Hp}} = 10^6$, $Re_{\text{Hp}} = 10^7$ and $d_e = 0$. A time series of six snapshots (A)–(F), each containing contour plots of the helical flux $\psi_* = \psi + r^2/(2q_s)$ and the electrostatic potential ϕ , is shown in Fig. 5. In the present case, the initial perturbation has triggered the first islands near the vertical (y) axis [Fig. 5(A)]. Their size corresponds roughly to $m = 8$, which is consistent with the fact that the $m = 8$ mode is the linearly fastest growing one in this setting (cf. Fig. 10 in Ref. [1]). The perturbation spreads out poloidally (B)–(E) towards the horizontal (x) axis. Eventually, the whole inter-resonance region is disrupted, predominantly by a nonlinear $m = 8$ DTM (D)–(F). The relaxation leads to a state with low magnetic shear in the former inter-resonance region (F). This can also be

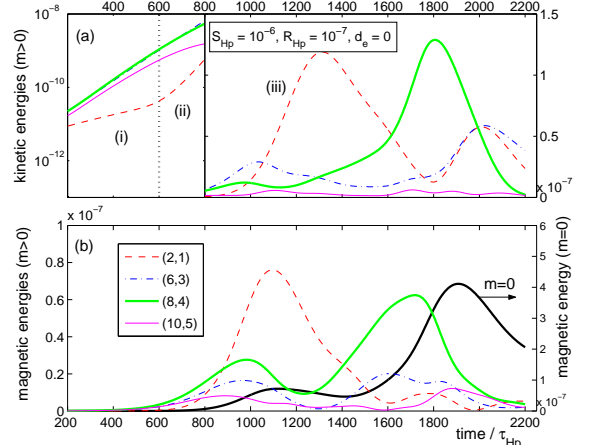


FIG. 7: (Color online). Collisional case. Evolution of (a) the kinetic and (b) the magnetic energies of the modes $(0, 0)$, $(2, 1)$, $(6, 3)$, $(8, 4)$ and $(10, 5)$. The three phases indicated in (a) are: (i) linear growth, (ii) nonlinearly driven growth of the $(2, 1)$ mode, and (iii) annular collapse phase.

observed in the evolution of the q profile shown in Fig. 6.

The temporal evolution of the kinetic energy ($E_{m,n}^{\text{kin}} = C_m \int dr r |\nabla \phi_{m,n}|^2$, $C_0 = 4\pi$, $C_{m>0} = 2\pi$) and the magnetic energy ($E_{m,n}^{\text{mag}} = C_m \int dr r |\nabla \psi_{m,n}|^2$) is shown in Fig. 7 for the modes $(m, n) = (0, 0)$, $(2, 1)$, $(6, 3)$, $(8, 4)$ and $(10, 5)$ [the profile perturbation $(0, 0)$ has only magnetic energy]. The labels (i) and (ii) in Fig. 7(a) indicate, respectively, the linear phase and the phase where the $(2, 1)$ mode undergoes nonlinear driving [30]. The fully nonlinear regime begins around $t = 800$ and the label (iii) indicates the annular collapse phase. Although the $(2, 1)$ mode has considerable kinetic and magnetic energy during the period $1000 \lesssim t \lesssim 1400$, the contour plots in Fig. 5 show that high- m islands are present at all times.

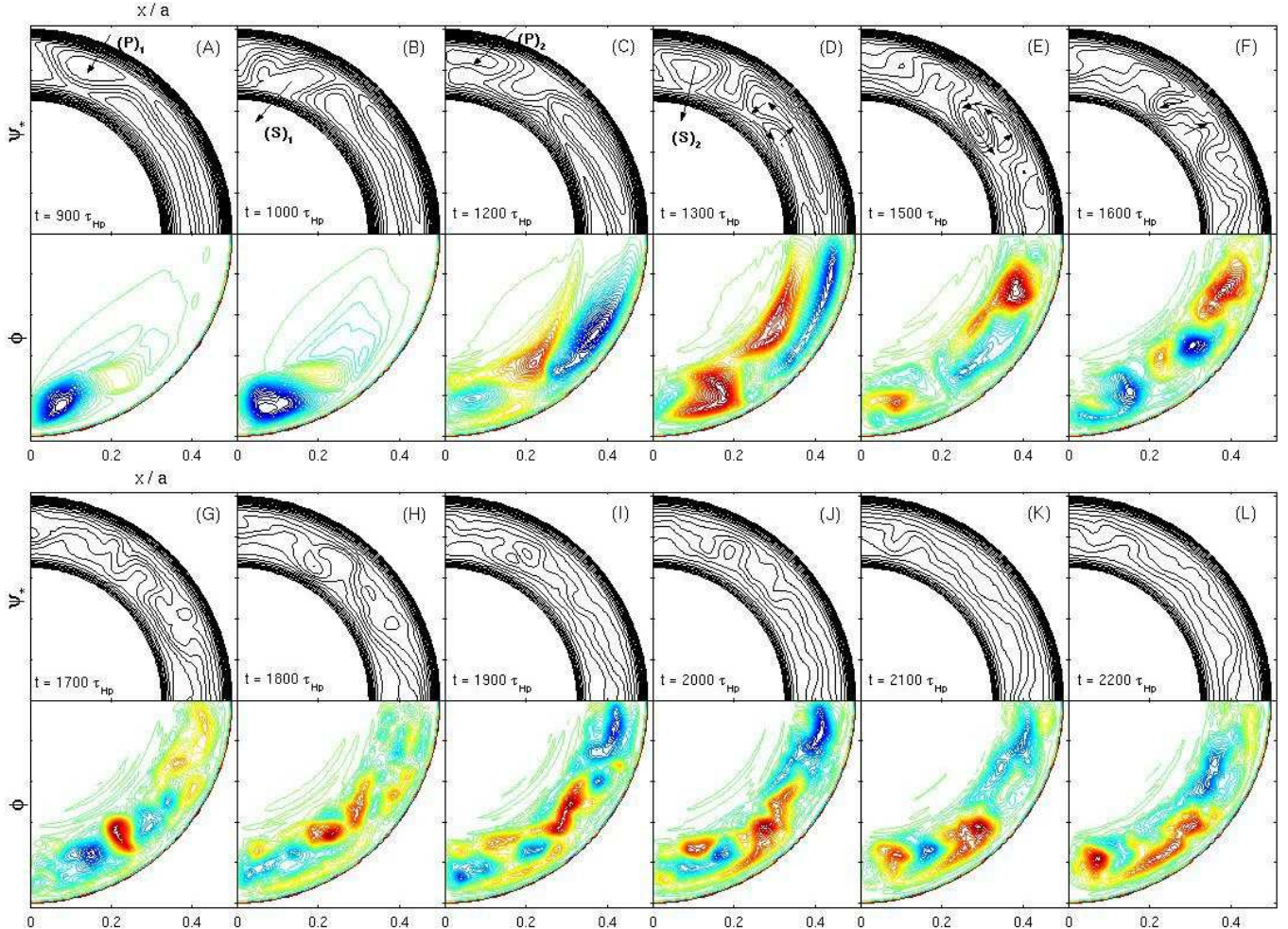


FIG. 8: (Color online). Collisionless case. Reconnection dynamics with $q_s = 2$ collisionless DTM for small inter-resonance distance $D_{12} = 0.06$. The twelve snapshots (A)–(L) were taken during the interval $900 \leq t \leq 2200$. Labeled arrows in (A)–(D) indicate primary (P) and secondary reconnection (S) events [first cycle: (A) and (B); second cycle: (C) and (D)]. Arrows in (D)–(F) highlight islands revolving around each other. Otherwise arranged as Fig. 5. Parameters: $S_{\text{HP}} = 10^8$, $Re_{\text{HP}} = 10^7$, $d_e = 0.01$.

The evolution of the magnetic energy of the $(0, 0)$ mode, $E_{0,0}^{\text{mag}}$ in Fig. 7(b), is closely linked to the evolution of the q profile in Fig. 6. $E_{0,0}^{\text{mag}}$ reaches its peak shortly after the $(8, 4)$ mode has grown to its maximum around $t = 1800$. At this point the $m = 8$ islands reach their maximal size [Fig. 5(E)] and the system has exhausted most of its free energy. Secondary reconnection (overshoot) occurs only in rudimentary form (E)–(F).

For $t > 2000$ the energy of the profile perturbation $E_{0,0}^{\text{mag}}$ decays. Correspondingly, the q profile does not rise further and tends to remain close to $q \approx 2$ in the region $r_{s1} \lesssim r \lesssim r_{s3}$. q_{\min} even drops back slightly below $q_s = 2$. This behavior is most likely due to the resistive decay of the profile perturbation $\tilde{\psi}_{0,0}$ because the resistive time scale τ_R for the inter-resonance region is comparable to the simulation time: $\tau_R(D_{12})/\tau_{\text{HP}} = \hat{\eta}^{-1} S_{\text{HP}} (D_{12}/2)^2 \sim 10^3$. Since the source term $S_{\text{HP}}^{-1} E_0$ in Eq. (2) maintains the original equilibrium profile the dissipation tends to

drive the system back to the initial unstable state. The system is expected to settle down in a state where the decay of $E_{0,0}^{\text{mag}}$ is balanced by weak MHD activity.

The nonlinear simulation for the collisionless case was carried out for the parameter values $S_{\text{HP}} = 10^8$, $Re_{\text{HP}} = 10^7$ and $d_e = 0.01$. The d_e value is just on the margin of the regime where it becomes comparable to the inter-resonance distance D_{12} (cf. Fig. 2). Although the resistivity is finite, it is small enough for its effect to be negligible for both the linear instability characteristics and the prominent features of the nonlinear dynamics.

Consider the sequence of twelve snapshots (A)–(L) shown in Fig. 8. As in the collisional case, the first islands appear near the y axis [Fig. 8(A)]. In accordance with the value of $m_{\text{peak}} = 8$ (cf. Fig. 2), the island sizes roughly correspond to $m = 8$. Primary and secondary reconnection events can be observed. Here, primary reconnection (P) is the process where an island forms. Dur-

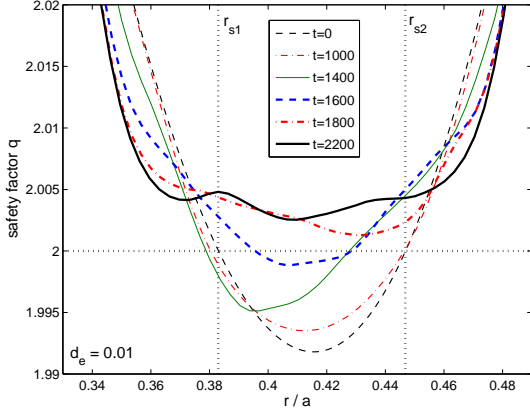


FIG. 9: (Color online). Collisionless case. Evolution of the q profile during the annular collapse.

ing the secondary reconnection (S) the island disappears at another location (usually on the opposite side of the inter-resonance region). We regard primary followed by secondary reconnection as one reconnection cycle. In Fig. 8 (A) and (B), one such cycle is indicated by arrows labeled $(P)_1$ and $(S)_1$. As can be seen in snapshots (C) and (D), the residual $\mathbf{E} \times \mathbf{B}$ flows in the upper part of the poloidal plane are strong enough to create another island $(P)_2$ which is also annihilated later through secondary reconnection $(S)_2$. Snapshots (D)–(F) reveal turbulent flows that cause islands to revolve around each other (arrows). In the following snapshots, (G)–(L), the magnetic islands gradually disappear. Turbulent small-scale flows can still be observed, but with significantly reduced energies.

A remarkable difference to the collisional case lies in the fact that after collisionless reconnection the inter-resonance region again has distinct flux surfaces [Fig. 8(F)]. As can be seen in Fig. 9, the q profile has changed (widened) outside the original $q_s = 2$ resonant surfaces and the relaxed state has $q > 2$ everywhere. The magnetic energy of the profile perturbation, $E_{0,0}^{\text{mag}}$ shown in Fig. 10(b), is found to rise relatively steadily to a level much higher than in the collisional case. Moreover, $E_{0,0}^{\text{mag}}$ seems to saturate rather than decay. This may again be understood in terms of the local resistive diffusion time, which is now much larger than the simulation time: $\tau_R(D_{12}) \sim 10^5$.

VI. DISCUSSION AND CONCLUSIONS

In tokamak plasmas with non-monotonic q profile pairs of nearby resonant surfaces with the same rational value $q_s = m/n$ are produced. Examples include the current ramp-up [31, 32], the current penetration after an internal disruption [33], and enhanced RS shear configurations where bootstrap current and external drive maintain an

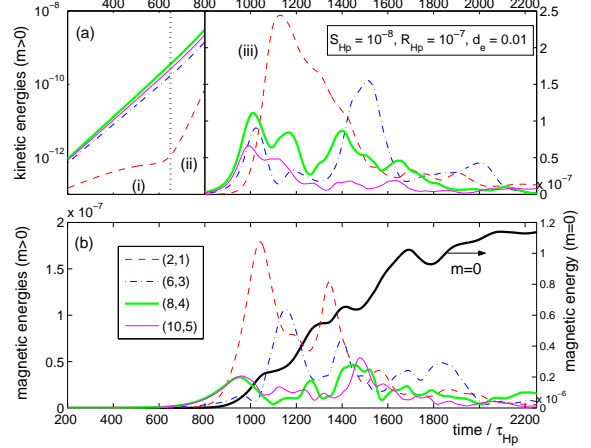


FIG. 10: (Color online). Collisionless case. Evolution of (a) the kinetic and (b) the magnetic energies of the modes $(0, 0)$, $(2, 1)$, $(6, 3)$, $(8, 4)$ and $(10, 5)$. The three phases indicated in (a) are: (i) linear growth, (ii) nonlinearly driven growth of the $(2, 1)$ mode, and (iii) annular collapse phase.

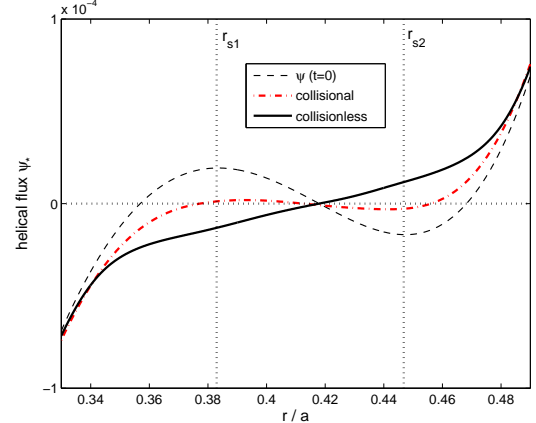


FIG. 11: (Color online). Helical flux profile $\psi_*(r)$ before and after the annular collapse in the collisional and collisionless case.

off-axis current peak (e.g., Ref. [16]). Motivated by the recent finding that high- m DTM s may be strongly unstable in such configurations shortly after q_{\min} drops below a low-order rational value [1, 12] we have analyzed the linear instability characteristics and nonlinear evolution of collisional and collisionless DTM s associated with a pair of nearby $q_s = 2$ resonant surfaces.

A comparison between the two cases showed that both can give rise fast growing DTM s with similar linear mode structure and high mode numbers $m \sim 10$. A random broad-band perturbation was shown to induce an annular collapse with small island structures, both in the collisional and collisionless case. This is in contrast to the situation typically found for large inter-resonance distances where the lowest- m modes dominate and produce large coherent island structures in the early stages of the non-

linear evolution (e.g., Refs. [8, 34]). The dominance of the fastest growing high- m modes survives far into the nonlinear regime. The detailed evolution depends on the initial conditions used in the calculation, i.e., the relative initial amplitudes of the modes and their phase relations [30]. The disruption may begin relatively localized poloidally (as in Figs. 5 and 8) or everywhere simultaneously. In any case, the final result, namely the disruption of the whole inter-resonance region, is independent of the initial perturbation. The disrupted region is characterized by reduced magnetic shear and MHD turbulence.

Due to the similarity of collisional and collisionless DTM s with respect to the properties mentioned above it may be conjectured that the dominance of high- m modes in configurations with sufficiently small inter-resonance distance is a common feature of DTM s regardless of the reconnection mechanism. However, there are also certain differences.

The nature of the reconnection mechanism does have an influence on the width of the spectrum of unstable modes. It was found that, with the same q profile, many high- m DTM s which are stable with resistive reconnection become unstable when the electron inertia effect dominates. This has the important implication that the instability of a DTM with given mode numbers (m, n) is not determined by the current profile alone, an observation which requires further investigation.

The reconnection and island dynamics in the collisional and collisionless case are fundamentally different from each other. After the annular collapse in the collisional case the profile perturbation decays rapidly due to the dissipative nature of the system. It is driven back towards

the initial unstable state, a tendency which is balanced by continued (weak) MHD activity. The relaxed helical flux profile $\psi_*(r)$ is flat in the inter-resonance region as can be seen in Fig. 11 (dash-dotted line). In contrast, the collisionless case passes through multiple cycles of primary and secondary reconnection, during which the energy of the profile perturbation continuously rises until it saturates nonlinearly. The relaxed state is stable as can be inferred from the helical flux profile in Fig. 11 (solid line).

The results for $q_s = 2$ DTM s are directly applicable to other values of q_s [12]. This includes cases with nearby $q_s = 1$ resonant surfaces for which the dynamics of resistive DTM s were recently described in Ref. [30].

The results presented in the present paper motivate further investigations using more realistic models. To check our conjecture that for small inter-resonance distances high- m DTM s may be unstable with any reconnection mechanism, it may be necessary to include finite-Larmor-radius (FLR) effects in the generalized Ohm's law [Eq. (1)]. This is because in a tokamak the ion sound radius ρ_s is usually larger, or at least comparable to the electron skin depth d_e . Furthermore, d_e is replaced by a beta-modified natural scale length d_s [35].

Acknowledgments

A.B. would like to thank S. Günter, S. Hamaguchi and S. Benkadda for fruitful discussions. Furthermore, he acknowledges the Max-Planck-Institut für Plasmaphysik Garching for its support and hospitality.

[1] A. Bierwage, S. Benkadda, S. Hamaguchi, and M. Wakatani, *Phys. Plasmas* **12**, 082504 (2005).

[2] M. Kikuchi, *Plasma Phys. Control. Fusion* **35**, B39 (1993).

[3] R. J. Goldston, S. H. Batha, R. H. Bulmer, D. N. Hill, A. W. Hyatt, S. C. Jardin, F. M. Levinton, S. M. Kaye, C. E. Kessel, E. A. Lazarus, et al., *Plasma Phys. Control. Fusion* **36**, B213 (1994).

[4] H. P. Furth, P. H. Rutherford, and H. Selberg, *Phys. Fluids* **16**, 1054 (1973).

[5] P. L. Pritchett, Y. C. Lee, and J. F. Drake, *Phys. Fluids* **23**, 1368 (1980).

[6] H. P. Furth, J. Killeen, and M. N. Rosenbluth, *Phys. Fluids* **6**, 459 (1963).

[7] B. Coppi, R. Galvao, R. Pellat, M. N. Rosenbluth, and P. H. Rutherford, *Fiz. Plazmy* **2**, 961 (1976), [Sov. J. Plasma Phys. **2**, 533 (1976)].

[8] R. B. White, D. A. Monticello, M. N. Rosenbluth, and B. V. Waddell, in *Proceedings of the Conference on Plasma Physics and Controlled Nuclear Fusion Research, Berchtesgaden, Germany, 1976* (International Atomic Energy Agency, Vienna, 1977), vol. 1, p. 569.

[9] M. Persson and R. L. Dewar, *Phys. Plasmas* **1**, 1256 (1994).

[10] Q. Yu, *Phys. Plasmas* **3**, 2898 (1996).

[11] Y. Ishii, M. Azumi, and Y. Kishimoto, *Phys. Rev. Lett.* **89**, 205002 (2002).

[12] A. Bierwage, S. Hamaguchi, M. Wakatani, S. Benkadda, and X. Leoncini, *Phys. Rev. Lett.* **94**, 065001 (2005).

[13] H. Ji, M. Yamada, S. Hsu, and R. Kulsrud, *Phys. Rev. Lett.* **80**, 3256 (1998).

[14] R. Numata and Z. Yoshida, *Phys. Rev. Lett.* **4**, 045003 (2002).

[15] F. M. Levinton, R. E. Bell, S. H. Batha, E. J. Synakowski, and M. C. Zarnstorff, *Phys. Rev. Lett.* **80**, 4887 (1998).

[16] S. Günter, S. Schade, M. Maraschek, S. D. Pinches, E. Strumberger, R. Wolf, Q. Yu, and the ASDEX Upgrade Team, *Nucl. Fusion* **40**, 1541 (2000).

[17] M. Ottaviani and F. Porcelli, *Phys. Rev. Lett.* **71**, 3802 (1993).

[18] D. Biskamp and J. F. Drake, *Phys. Rev. Lett.* **73**, 971 (1994).

[19] M. Ottaviani and F. Porcelli, *Phys. Plasmas* **2**, 4104 (1995).

[20] B. Coppi, *Phys. Rev. Lett.* **12**, 417 (1964).

[21] Q. Yu, S. Günter, and B. Scott, *Phys. Plasmas* **10**, 797 (2003).

[22] H. R. Strauss, *Phys. Fluids* **19**, 134 (1976).

- [23] K. Nishikawa and M. Wakatani, *Plasma Physics* (Springer, Berlin, 2000).
- [24] H. R. Strauss, Phys. Fluids **29**, 3668 (1986).
- [25] J. Q. Dong, S. M. Mahajan, and W. Horton, Phys. Plasmas **10**, 3151 (2003).
- [26] P. K. Kaw, E. J. Valeo, and P. H. Rutherford, Phys. Rev. Lett. **43**, 1398 (1979).
- [27] A. Y. Aydemir, Phys. Fluids B **2**, 2135 (1990).
- [28] S. M. Mahajan and R. D. Hazeltine, Nucl. Fusion **22**, 1191 (1982).
- [29] A. Bierwage, S. Benkadda, S. Hamaguchi, and M. Wakatani, Phys. Plasmas **13**, 032506 (2006).
- [30] A. Bierwage, S. Benkadda, S. Hamaguchi, and M. Wakatani,
- Preprint: <http://arxiv.org/abs/physics/0609102>.
- [31] J. Schmidt and S. Yoshikawa, Phys. Rev. Lett. **26**, 753 (1971).
- [32] T. H. Stix, Phys. Rev. Lett. **36**, 521 (1976).
- [33] R. G. Kleva, Phys. Fluids B **4**, 218 (1992).
- [34] Y. Ishii, M. Azumi, G. Kurita, and T. Tuda, Phys. Plasmas **7**, 4477 (2000).
- [35] T. J. Schep, F. Pegoraro, and B. N. Kuvshinov, Phys. Plasmas **1**, 2843 (1994).
- [36] The q profile in Fig. 1 can be reproduced using the model formula (11) in Ref. [1], with the parameter values of Case (IIIb) in that reference.